J Mater Sci: Mater Electron (2021) 32:21124–21134

Influence of mechanical alloying on structural, thermal, and magnetic properties of $Fe_{50}Ni_{10}Co_{10}Ti_{10}B_{20}$ high entropy soft magnetic alloy

Mrutyunjay Panigrahi[1] and Baris Avar[2,*]

[1] School of Mechanical Engineering, Vellore Institute of Technology, Chennai, Tamil Nadu 600127, India
[2] Department of Metallurgical and Materials Engineering, Zonguldak Bulent Ecevit University, Incivez, 67100 Zonguldak, Turkey

Received: 24 May 2021
Accepted: 11 July 2021
Published online: 16 July 2021

ABSTRACT

A multicomponent with functional $Fe_{50}Ni_{10}Co_{10}Ti_{10}B_{20}$ (at.%) high entropy soft magnetic alloy powders were produced from the elemental powders by mechanical alloying (MA). The MA processes were carried out under argon gas atmosphere at a speed of 250 rpm, carrying milling and rest in every 20-min period to prevent the mixture from overheating. Scanning electron microscopy and energy-dispersive X-ray spectroscopy, X-ray diffraction, differential thermal analysis, and vibrating sample magnetometer analysis were utilized to characterize various powdered samples with respect to MA time (0–50 h). The results show that in the first 2.5 h of MA, the mixture of crystalline phases transformed into a nanocrystalline supersaturated α-Fe solid solution phase. With prolonging milling time, the amorphous phase appeared after 20 h of MA. In the final stage of MA (50 h), the saturation magnetization (Ms) and the coercivity (Hc) were 89.7 emu/g and 32.5 Oe, respectively, proposing the alloy as a very good high entropy soft magnet in nature.

1 Introduction

The preparation of high entropy alloys (HEAs) using effective technology is critical for modern society. The demands of HEAs which are known as novel metallic functional materials are growing day by day and attract considerable attention for its low cost, miniature size, very long lasting, and environment friendly [1, 2]. HEAs have tremendous prospective in the field of engineering application at high temperature, biomedicine, and applications in the medical industry [3, 4]. The basic idea of HEA was initiated from expanding the number of elements to enhance the mixing entropy of the alloy to reach the objective of the formation of a stable solid solution alloy [5, 6]. These are also known as multi-principal element alloys (MPEAs) or compositionally complex alloys (CCAs) [4, 7]. Depending on the multiple elements, HEAs are a novel class of alloys that provide improved performance by adjusting the composition and managing the process, where the phase composition is transformed from a single-phase solid

Address correspondence to E-mail: barisavar@beun.edu.tr; barisavar@gmail.com

https://doi.org/10.1007/s10854-021-06612-z

solution to several complex phase compositions. Furthermore, material scientists have classified the HEAs into two major groups and investigated their deformation mechanisms [1]. The first group is classified according to the crystallographic phase structure as BCC, FCC, and HCP-based, amorphous, and intermetallic HEAs. In contrast, the second group is classified based on the type of phase such as single, dual, eutectic, and multi-phase HEAs [1].

In this context, the HEAs have attracted considerable attention because of their superior features, such as high strength and structural stability, low-temperature performance, good corrosion, wear, and oxidation resistance, and so on [8–12]. To increase the amorphous forming of the composition, various magnetic materials with nanocrystalline structure have been prepared by mixing of late transition metals, such as Fe, Co, and Ni; early transition metals. such as Ti, Zr, and Nb; and metalloids such as B, P, and Si, [3, 13, 14].

The HEAs can be prepared by several methods. From which, powder metallurgy, ingot metallurgy, and selective laser melting are the commonly utilized approaches to synthesize as bulk form, whereas laser cladding and magnetron sputtering are generally utilized to synthesize as thin film or coating form [1].

However, in this research, the Fe-based HESM alloys were prepared using the MA process with high-energy mills because of its simple nature, reasonably low-cost, and controlled process parameters [3, 15]. The MA is an efficient powder production method to create an extensive range of stable and metastable materials such as intermetallics, supersaturated solid solution, nanocrystalline, quasicrystalline, and amorphous alloys. This method includes repeated fragmentation and welding of component particles [16]. Currently, various types of mills are used for MA including planetary ball mills, attritors, shaker, and vibrating and rod mills, besides innovative designs that have been generated recently for functional occasions [17]. However, the high-energy planetary ball mill was used in this study due to the capable of high speed and rapidly effecting MA.

Although, there are so many advantages of the MA process, powder contamination is a critical limitation [18]. The chemical purity of the used powders, process control agents (PCA), milling tools, and atmosphere, all contribute to powder contamination [19]. One possibility way to reduce contamination from the milling tools is to use the same material as the powder being milled. If the powder material is not the same as the milling vials, and balls, a thin coating with the powders on the interior surface of the vial can be performed to reduce contamination [20]. Therefore, in this study, the milling container was properly sealed, and inert gas was used as a surrounding atmosphere to overcome the contamination.

Amorphous magnetic alloys, magnetic multilayers, granular alloy, and others have recently received much more attention due to their unique features and uses in transformers, generators, and sensors [21]. The reduced magnetostriction and magnetocrystalline anisotropy in the Co-based amorphous alloys lead to the low coercivity, high permeability, and low hysteresis losses properties [22].

The present work was taken up with the intention of developing a Fe-based HESM amorphous alloys targeting to reduce the application of the valuable alloying elements with high thermal stability. It is common that the soft magnetic properties of the material can be improved by varying the microstructure and decreasing the crystallite size [23, 24]. The random anisotropy model renders the theoretical basis for understanding the soft magnetic properties of the material. The improvement of soft magnetic properties can take place because of the averaging effect of magnetocrystalline anisotropy, while the size of the particle forms smaller than the magnetic exchange length [3, 25, 26].

Most of the alloys were prepared commercially with one or two principal elements, the near equiatomic characteristics of HEAs are expensive because of the enormous amount of additions of valuable alloying elements, such as Ta, V, Nb, and Zr, restricts their commercial uses [5]. Therefore, reducing the cost of HEAs has become one of the key points in the growth and application of new HEAs. This new class of alloy and its current idea can break the bottleneck of the traditional design of the material and generate new concepts for research and development of the more efficient functional metallic materials. Thus, the design of Fe-based HESM alloys with excellent properties is of tremendous significance for the growth of the application of high-temperature environment.

2 Strategy of the alloy design

Pure iron (Fe) was decided to use as a primary constituent to decrease the total cost of the HESM alloys. Pure Fe is an excellent low resistive ferromagnetic material. However, it shows a high loss of eddy current in high-frequency electronic devices. While it forms alloy, a high magnetic permeability and low total loss can be attained establishing the efficiency of the device more [3, 27, 28]. Nickel (Ni) was utilized as the FCC forming element to achieve proper FCC phase to provide the ductility, γ-stabilizer in ferrous alloys [5]. Due to the above-observed enhancement, it motivated the authors to prepare various Fe-based HESM alloys. Moreover, the Cobalt (Co) addition in Fe-based HESM alloys is familiar to form intermetallic forming elements. It can also help to enhance the Curie temperature and forms HITPERM alloys which is an appropriate candidate for designing the materials for particular purposes such as high-temperature applications [3, 13]. Addition of Titanium (Ti) to the HESM alloys is beneficial for strength and compressive ductility. However, the corrosion resistance of the HESM alloys can increase with the addition of Ti content [29]. For metalloids such as Boron (B), an inexpensive material can be added to the Fe-based HESM alloys to increase the wear resistance and hardness by the formation of borides [30, 31]. However, increase in the addition of B in the Fe-based HESM alloys indicate the decrease of the corrosion resistance property [32].

In view of the above, the development of a new Fe-based material is very urgent, and the emergence of Ni, Co, Ti, and B is expected to meet the actual soft magnetic needs. It was reported that a novel $(FeCoNi)_{70}Ti_{10}B_{20}$ (at.%) alloy was prepared (Avar et al.) using MA from various elemental powders such as Fe, Co, Ni, Ti, and B [3]. The main focus of the research was to develop a stable amorphous-phase alloy to use for quality application such as a soft-core magnetic material [3]. In view of the above, the soft magnetic HEAs were prepared by reducing the intermetallic forming element (Co) content and increasing the FCC forming elements (Fe and Ni) content correspondingly. However, only the Fe content was increased and the Ni content was fixed at 10 at.% as Fe is cheaper than Ni. Hence, the aim was to lower the total cost of the soft magnetic alloy. Taking intoabove consideration, the $Fe_{50}Ni_{10}Co_{10}Ti_{10}B_{20}$ (at.%) category of Fe-based HESM alloys was therefore designed.

3 Experimental procedure

Pure elemental powders were mixed to give a nominal composition of $Fe_{50}Ni_{10}Co_{10}Ti_{10}B_{20}$ (at.%) HESM alloys. MA process was carried out in a high-energy planetary ball mill, under argon atmosphere, using hardened steel balls and vial. The powder-to-ball weight ratio and the rotation speed were maintained as 1:10, 250 rpm, respectively. Every 20 min of MA process was followed by a suspension of 20 min to prevent excessive heating. Thus, the rotational direction of the equipment was changed anti-clockwise/clockwise after every 40 min of interval to enhance the efficiency. The MA process was interrupted at predetermined intervals and a small amount of HESM alloy powder was taken for further characterization. The structural transformation and the phase recognition were analyzed by X-ray diffraction (XRD) using a Panalytical Empyrean diffractometer with CuKα radiation generated at 45 kV and 40 mA. The XRD analyses were utilized from 10°–90° (2θ) with a step size of 0.013° and a count time of 48.1950s/step. The morphological change of the powder particles was analyzed by a scanning electron microscopy and energy-dispersive X-ray spectroscopy (SEM/EDX) using a FEI-Quanta FEG 450 microscope operated at 15 kV in secondary electron mode. The average powder particle size was evaluated from the SEM micrographs using ImageJ tool software. The thermal behavior of the milled powders was determined by differential thermal analysis (DTA) using a SII Exstar TG/DTA 7200 in flowing N_2 atmosphere, temperature in the range of 300–950 °C at a heating rate of 20 °C/min. The magnetic characterizations were performed by using a vibrating sample magnetometer (VSM) (Lake Shore 7407) at 23 °C within ± 15 kOe magnetic field ranges.

4 Results and discussion

4.1 Morphology and particle size

The SEM micrographs of the initial raw material powders such as Fe, Co, Ni, Ti, and B are presented in Fig. 1. The SEM micrographs revealed that the initial

raw material powders contain the irregular shapes of Ti and B, pellet types of Fe, spherical shape of Co, and cuboid type of morphology of Ni, respectively. The SEM micrographs of the particle evolution of the $Fe_{50}Ni_{10}Co_{10}Ti_{10}B_{20}$ HESM alloys with respect to various milling time are presented in Fig. 2. Initially, the particle size was increased while milling the material powders at 2.5 h due to the agglomeration of different constituents and later decreased gradually. The typical mechanism of multicomponent systems during MA is flattened of the ductile components due to the high plastic deformation, cold welding, and fracturing of the brittle components [3, 18]. These effects change the morphology, particle size, and microstructure of the material powders. Moreover, the size of the HESM alloys particles becomes smaller with the increase in the milling duration up to 5–10 h and the particles of the HESM alloys obtain the smallest size of 5–25 μm. By prolonging the milling time of the material powders up to 20 h, the particle size was increased again due to the sticking of the particles on the wall and the grinding balls [3, 33]. After 40 h of milling, the microstructures of the powders reveal that a lower energy transfer into the powders greatly decreased the MA progression. Then the milling time was increased up to 50 h to achieve the spherical homogeneous powder particles of 5–15 μm and supersaturated solid solutions.

The average particle size variation of the HESM alloy powders with respect to the milling duration calculated from the SEM micrographs using the ImageJ tool software is shown in Fig. 3. The obtained results show that the particle size is decreasing with the increase in milling time. It was noted that the average particle size of the initial powder without milling was around 12 μm. However, the average particle size was increased up to 41 μm while milling at 2.5 h. The increase of the average mixed powder particle size during the initial time of the MA was due to substantial particle deformation, as well as the development of new surfaces and subsequent cold-welding processes, especially the ductile constituents present in the mixed powder compositions. The analysis of the particle size variation points out that after 5 h of the MA, the average particle size was decreased up to 19 μm. This is due to the cracking of the powder particles created by the deformation strengthening. Then by stretching the duration of milling to 20 h, the average particle size increased up to 29 μm. This is probably due to the high-energy ball milling; the powder particles are flattened, fragmented, and rewelded several times. When two hardened steel balls collide, a sum of powder is trapped between them. This plastically deforms the powder particles, creating new surfaces and allowing them to fuse together, resulting in a particle size increase [17, 19]. With increasing the milling duration up to 40 h, the average particle sizes decreased up to 12 μm and with extended milling time further, the particles were finer and spherical and indicated the completion of the amorphization process in the solid state [3, 18].

Figure 4 exhibits the energy-dispersive X-ray spectroscopy analysis (EDX) elemental mapping of the 50-h milled $Fe_{50}Ni_{10}Co_{10}Ti_{10}B_{20}$ HESM alloy powder. Uniform and homogeneous distribution of the Fe, Co, Ni, Ti, and B in the $Fe_{50}Ni_{10}Co_{10}Ti_{10}B_{20}$ HESM alloy powder was observed. It was also indicated that the $Fe_{50}Ni_{10}Co_{10}Ti_{10}B_{20}$ HESM alloy powders were not contaminated from the atmosphere and the milling media as there was no other elemental impurity including oxygen was traced.

4.2 XRD analysis

The XRD patterns of the initial powder mixture without milling are shown in Fig. 5. The characteristic high-intensity crystalline peaks for the Fe phases (JCPDS No. 98-007-6747), Co (JCPDS No. 98-004-4989), Ni (JCPDS No. 98-064-6092), and Ti (JCPDS No. 98-005-2522) were distinctly recognized. Furthermore, the diffraction peaks of B were not monitored because of its low atomic scattering factor, and amorphous nature [3, 18].

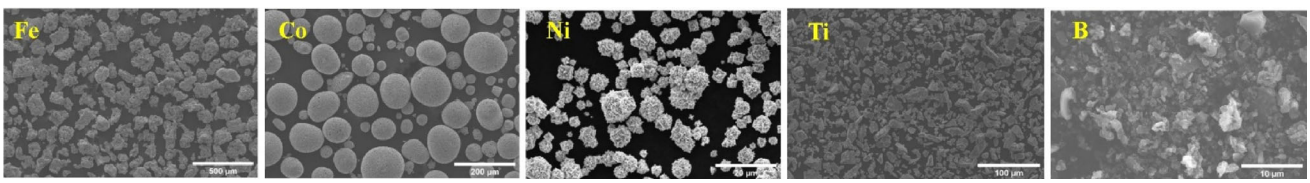

Fig. 1 SEM micrographs of the individual constituents: Fe, Co, Ni, Ti, and B, used in the initial powder mixture

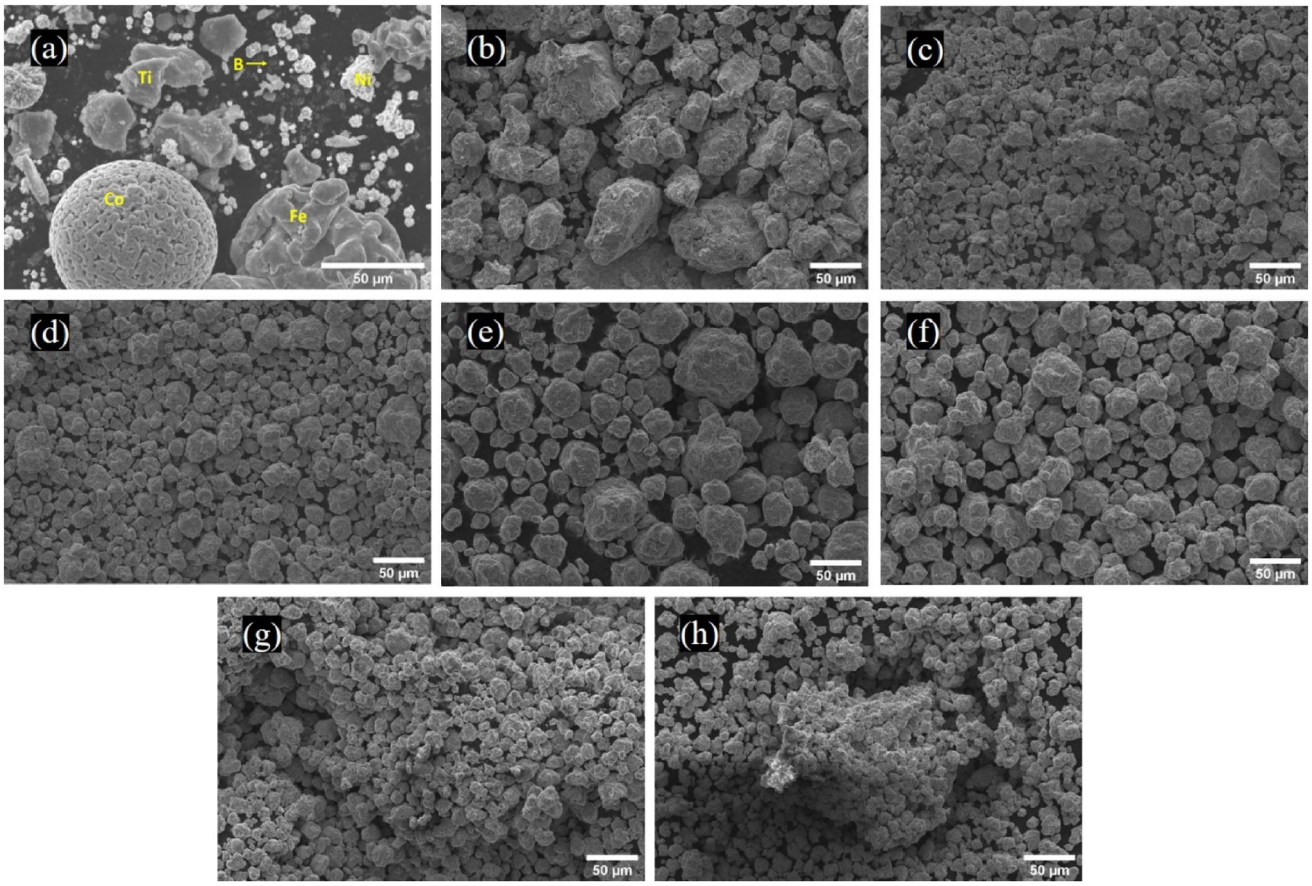

Fig. 2 SEM micrographs of the milled powders at different milling times in h: **a** 0, **b** 2.5, **c** 5, **d** 10, **e** 20, **f** 30, **g** 40, and **h** 50

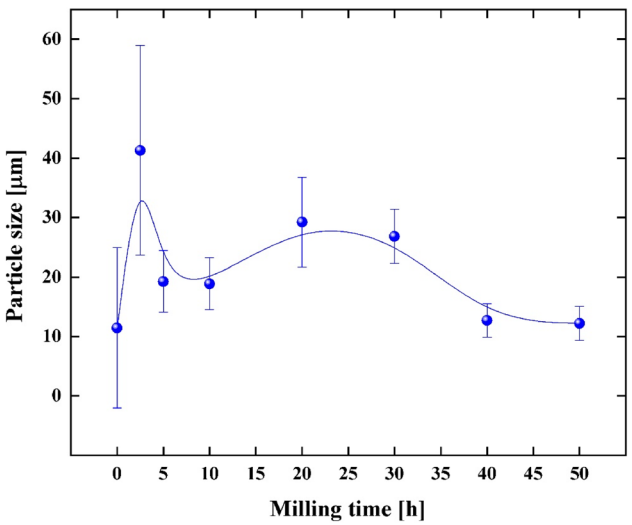

Fig. 3 Average particle size variation with respect to the milling time during the MA process

The XRD patterns of the $Fe_{50}Ni_{10}Co_{10}Ti_{10}B_{20}$ HESM alloys (at.%) powders prepared at the predefined milling times are shown in Fig. 5. The gradual changes of XRD patterns clearly show the existence of structural transformation of the $Fe_{50}Ni_{10}Co_{10}Ti_{10}B_{20}$ HESM alloy powders milled for a period of 2.5–50 h. It was observed that three Bragg peaks were identified including a sharp peak, which corresponds to FCC structure at the early milling stage (2.5–10 h). It was noticed that the two peaks were disappeared after milling at 20 h and the much higher diffraction intensity peak of the $Fe_{50}Ni_{10}Co_{10}Ti_{10}B_{20}$ HESM alloy powders was predominant in the alloy. As illustrated in Fig. 5, the sharp peak noticed around at 44.38° was slightly shifted towards higher angle and the intensity of the peak was decreased. Prolonging the milling time up to 20 h, the peak width becomes much broader, and this is ascribed to the initiation of the formation of solid solution with a decrease in grain size and an increase in lattice strain, suggesting the decrease of crystallinity [3, 18]. This indication also predicted the early stages of amorphization of solid solution phase. The peak intensity gradually becomes weaker and weaker with diminished intensity with respect to the increased milling time. After further

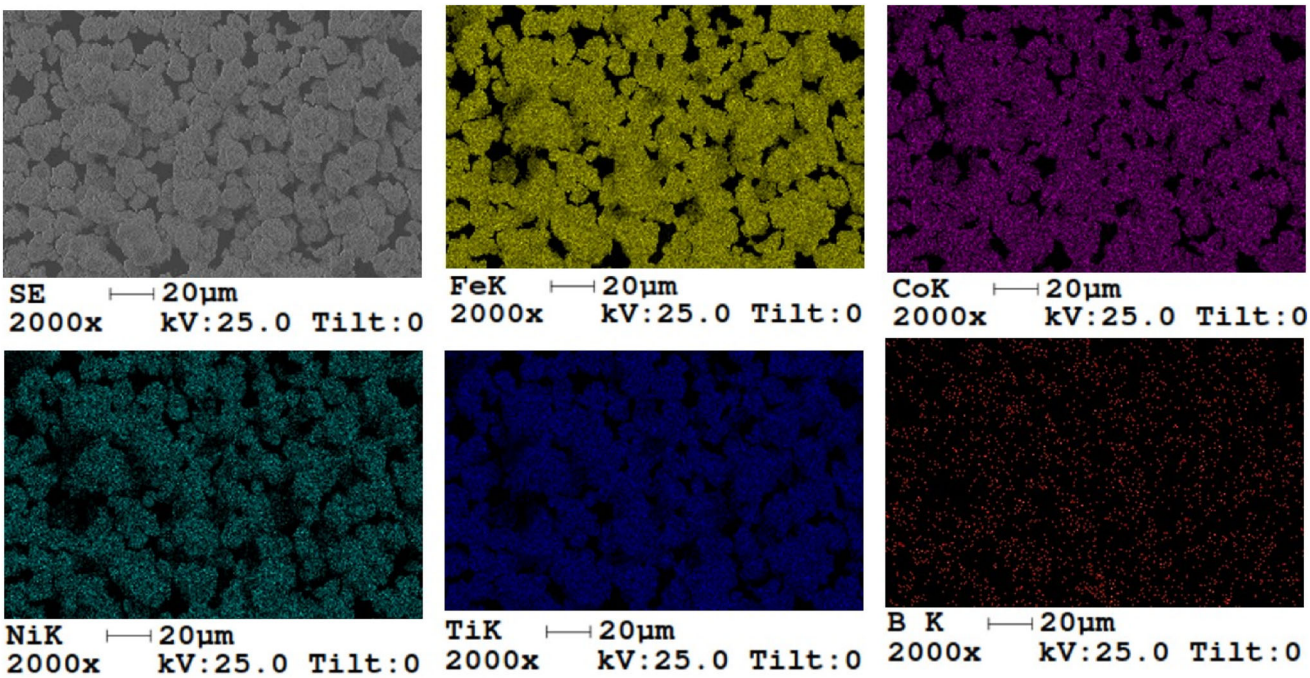

Fig. 4 EDX elemental mapping of the 50-h milled $Fe_{50}Ni_{10}Co_{10}Ti_{10}B_{20}$ HESM alloy powder

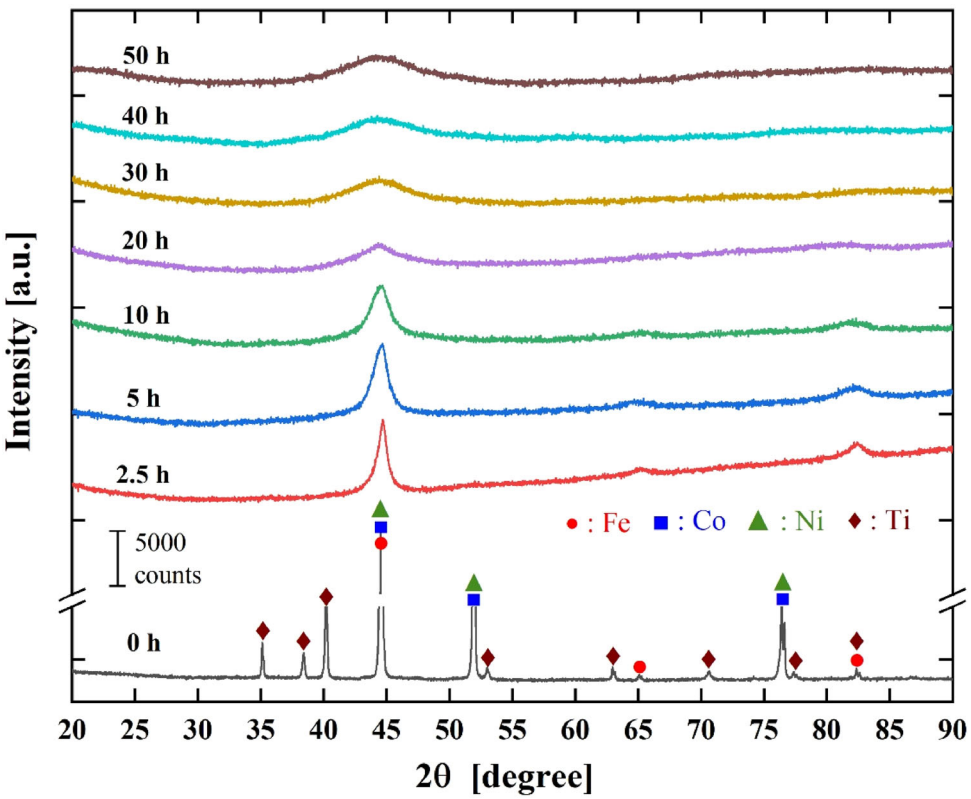

Fig. 5 XRD patterns of the initial powder mixture and the $Fe_{50}Ni_{10}Co_{10}Ti_{10}B_{20}$ HESM alloys as a function of milling time

increase of the milling duration up to 50 h, all crystalline peaks disappear and only a broad hump exists which estimates the formation of a high percentage of amorphous phase-like structure of the $Fe_{50}Ni_{10}Co_{10}Ti_{10}B_{20}$ HESM alloy powders [6]. These results indicate that the $Fe_{50}Ni_{10}Co_{10}Ti_{10}B_{20}$ HESM alloy

powders were mechanically alloyed which encounters a composition modulation during the initial period of early milling stages, and then the compositionally modulated phase becomes amorphized as the milling time increased [18].

4.3 Thermal analysis

The DTA curves of the $Fe_{50}Ni_{10}Co_{10}Ti_{10}B_{20}$ HESM alloy powders with respect to various milling time are shown in Fig. 6. It was observed that there was no thermal peak traced while milling the mixed powders up to 2.5 h. However, there was one distinct exothermic peak traced at around 642 °C, which indicates the formation of different metastable phases as the milling duration of the mixed powders increases. As the milling time of the mixed powders increases up to 20 h, an additional broad peak was traced at lower temperature around 542 °C in addition to the distinct peak traced at around 642 °C, which suggest the transformation of the amorphous phase from the α-Fe solid solution phase during continuous heating. There is a slight variation of the broad exothermic peak from 542 °C for the 20 h to 556 °C for the 50-h milled $Fe_{50}Ni_{10}Co_{10}Ti_{10}B_{20}$ HESM alloy powder. This is probably due to the continuous changes in the chemical composition of the HESM alloys. It was observed that while milling the mixed powders for longer time up to 50 h, the distinct peak shifted towards lower temperature with reduced intensity. However, the broad peak was shifted towards higher temperature with higher intensity. It suggests the conversion of the metastable phases and the amorphous phases to crystallinity or more crystallization occurs [3, 6, 18].

To understand the above thermal behavior in detail, the 50-h milled $Fe_{50}Ni_{10}Co_{10}Ti_{10}B_{20}$ HESM alloy powder was again heat treated in the DTA furnace with a heating rate of 40 °C/min at various temperatures followed by rapid cooling to room temperature to understand the extent of transition from the amorphous to crystalline phase during each thermal stage. Figure 7 shows the XRD patterns of the 50-h milled $Fe_{50}Ni_{10}Co_{10}Ti_{10}B_{20}$ HESM alloy powder with respect to various temperatures at 300, 500, and 700 °C, respectively. It seems that the heat treatment below 300 °C could not persuade sufficient crystallinity and looks almost similar to the original 50-h milled powder. However, the crystallization of the $Fe_{50}Ni_{10}Co_{10}Ti_{10}B_{20}$ HESM alloy powder seemed to have initiated only after 300 °C, indicating the presence of a broad peak of short-range order with low intensity. However, a sharp peak of long-range order with high intensity was seen, while the $Fe_{50}Ni_{10}Co_{10}Ti_{10}B_{20}$ HESM alloy powder was heated at 500 °C. The peak of α-Fe (JCPDS No. 98-018-5748) phase was present in the $Fe_{50}Ni_{10}Co_{10}Ti_{10}B_{20}$ HESM alloy powder. After the $Fe_{50}Ni_{10}Co_{10}Ti_{10}B_{20}$ HESM alloy powder was heat treated at 700 °C, several crystalline phases of long-range order, regular patterns of particle arrangement, which repeats itself periodically were obtained over the entire crystal.

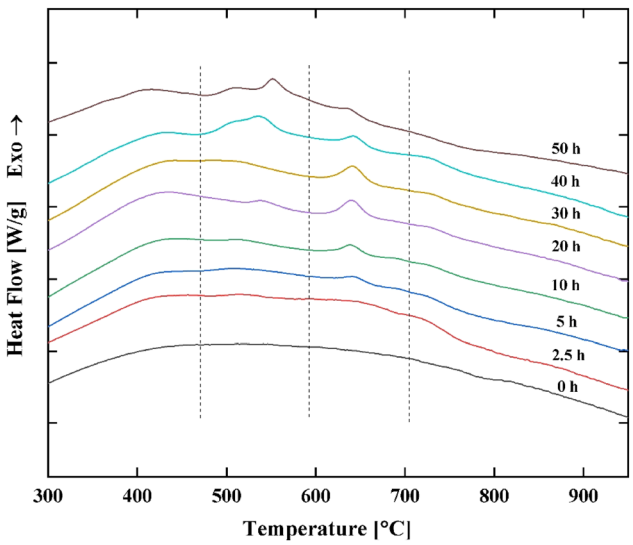

Fig. 6 DTA curves of the $Fe_{50}Ni_{10}Co_{10}Ti_{10}B_{20}$ HESM alloy powders for various milling time

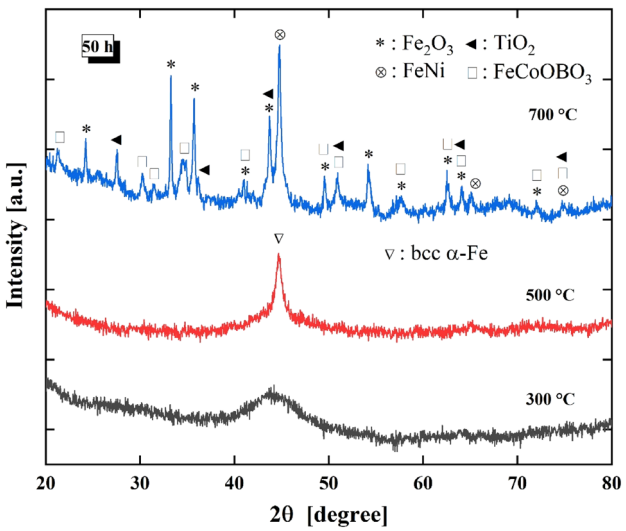

Fig. 7 XRD patterns of the 50-h milled $Fe_{50}Ni_{10}Co_{10}Ti_{10}B_{20}$ HESM alloy powder with respect to various temperatures

The crystalline phases such as Fe_2O_3 (JCPDS No. 98-041-5251), TiO_2 (JCPDS No. 01-078-1510), FeNi (JCPDS No. 00-037-0474), and $FeCoOBO_3Ti$ (JCPDS No. 01-070-1576) were clearly identified.

4.4 Magnetic properties

The magnetic properties of the $Fe_{50}Ni_{10}Co_{10}Ti_{10}B_{20}$ HESM alloy powder were characterized using vibrating sample magnetometer (VSM). A hysteresis curve of the 2.5, 10, 30, and 50-h milled $Fe_{50}Ni_{10}Co_{10}Ti_{10}B_{20}$ HESM alloy powder was plotted by magnetization (*M*) vs applied magnetic field (*H*) which is shown in Fig. 8. It was observed from Fig. 8 that all powders exhibit soft magnetic nature. Figure 9 shows the saturation magnetization (Ms) and coercivity (Hc) of the $Fe_{50}Ni_{10}Co_{10}Ti_{10}B_{20}$ HESM alloy powders with respect to various milling time. It shows that the Ms of the milled $Fe_{50}Ni_{10}Co_{10}Ti_{10}B_{20}$ HESM alloy powder of 2.5, 10, 30, and 50 h was determined as 86.5, 108.6, 27.0, and 89.7 emu/g, respectively. It is observed that the milled $Fe_{50}Ni_{10}Co_{10}Ti_{10}B_{20}$ HESM alloy powder at 10 h demonstrates the high Ms value of 108.6 emu/g which contains the α-Fe solid solution phase. Further increasing the milling time of the $Fe_{50}Ni_{10}Co_{10}Ti_{10}B_{20}$ HESM alloy powder at 50 h exhibits the amorphous phase [34]. The Hc of the milled $Fe_{50}Ni_{10}Co_{10}Ti_{10}B_{20}$ HESM alloy powder of 2.5, 10, 30, and 50 h was determined as 38.8, 59.2, 33.0, and 32.5 Oe, respectively. A sharp decrease in Hc value is observed in the $Fe_{50}Ni_{10}Co_{10}Ti_{10}B_{20}$ HESM alloy powder with respect to

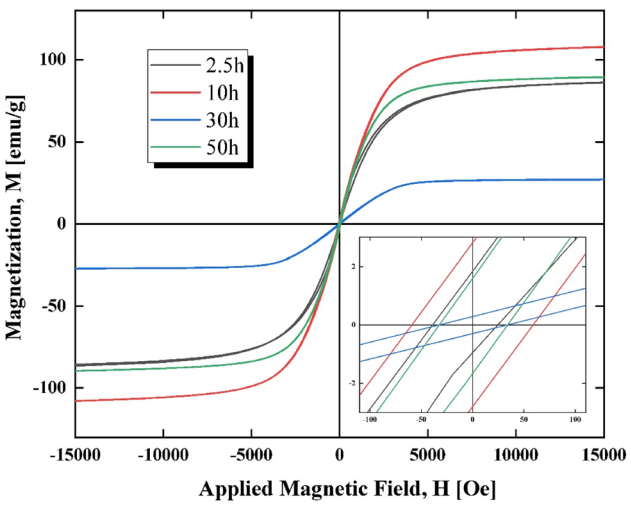

Fig. 8 *M–H* hysteresis curves of the milled $Fe_{50}Ni_{10}Co_{10}Ti_{10}B_{20}$ HESM alloy powder at 2.5, 10, 30, and 50 h

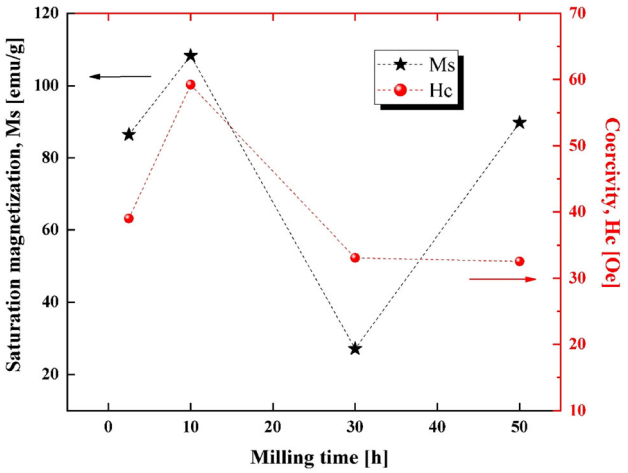

Fig. 9 Saturation magnetization and coercivity of the $Fe_{50}Ni_{10}Co_{10}Ti_{10}B_{20}$ HESM alloy powders with respect to various milling time

various milling time. It indicates the soft magnetic character of the $Fe_{50}Ni_{10}Co_{10}Ti_{10}B_{20}$ HESM alloy powder due to the release of the milling-induced internal stress with high saturation magnetization and low coercivity [3, 18, 35]. This can also be associated with the variation of the interatomic spacing in the grain boundaries with respect to the crystalline phases of the alloy.

Further, the 50-h milled $Fe_{50}Ni_{10}Co_{10}Ti_{10}B_{20}$ HESM alloy powder heat treated at 300, 500, and 700 °C was analyzed by VSM to recognize the influence of heat treatment on magnetic behavior. A hysteresis curve of the 50-h milled $Fe_{50}Ni_{10}Co_{10}Ti_{10}B_{20}$ HESM alloy powder without heat treated and with heat treated at 300, 500, and 700 °C was plotted by *M* vs *H*, and is shown in Fig. 10, which exhibits soft magnetic nature. However, Fig. 11 shows the Ms and Hc of the 50-h milled $Fe_{50}Ni_{10}Co_{10}Ti_{10}B_{20}$ HESM alloy powder with respect to various temperatures. It shows that the Ms was determined as 101.9, 71.0, and 38.3 emu/g, and while heat treated, the 50-h milled $Fe_{50}Ni_{10}Co_{10}Ti_{10}B_{20}$ HESM alloy powder at 300, 500, and 700 °C respectively. However, the Hc was determined as 13.3, 14.5, and 72.2 Oe, and while heat treated, the 50-h milled $Fe_{50}Ni_{10}Co_{10}Ti_{10}B_{20}$ HESM alloy powder at 300, 500, and 700 °C respectively. It was observed that the saturation magnetization significantly increases to 101.9 from 89.7 emu/g. This was observed because of the increase of ordering of the ferromagnetic property with decrease in the residual stress. However, higher heat treatment

temperature of 700 °C leads to low magnetic saturation with fully crystallization. The Hc value (72.2 Oe) was increased remarkably in the heat-treated $Fe_{50}Ni_{10}Co_{10}Ti_{10}B_{20}$ HESM alloy powder with respect to various temperatures. This is probably due to the grain growth during the course of heat treatment process. While the grain size is smaller than the magnetic exchange length, the effect of domain wall is decreased and each grain acts as a single domain [16].

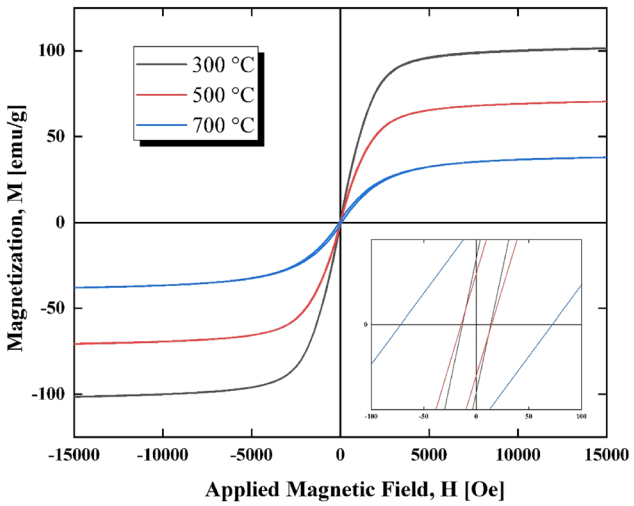

Fig. 10 *M–H* hysteresis curves of the 50-h milled $Fe_{50}Ni_{10}Co_{10}Ti_{10}B_{20}$ HESM alloy powder heat treated at 300, 500, and 700 °C

5 Conclusions

The preparation of $Fe_{50}Ni_{10}Co_{10}Ti_{10}B_{20}$ HESM alloy of nominal chemical composition by MA from a mixture of elemental powders such as Fe, Co, Ni, Ti, and B, resulted in the formation of a distinctive stable phase. It was observed that the structural disordering was enhanced with increasing the milling time, resulting in the structural stability of the amorphous phase. The highlight of the research is that the crystalline phases of the $Fe_{50}Ni_{10}Co_{10}Ti_{10}B_{20}$ HESM alloy were successively decreased and amorphism nature was enhanced with respect to the milling duration. The SEM micrographs confirmed that the particle size of the $Fe_{50}Ni_{10}Co_{10}Ti_{10}B_{20}$ HESM alloy powder was 12 μm. It was also observed that the morphology of the alloy powder was homogeneous, amorphous, and spherical in nature. The EDX mapping analysis indicated that the full homogeneity of the elemental powders, implying an excellent solid

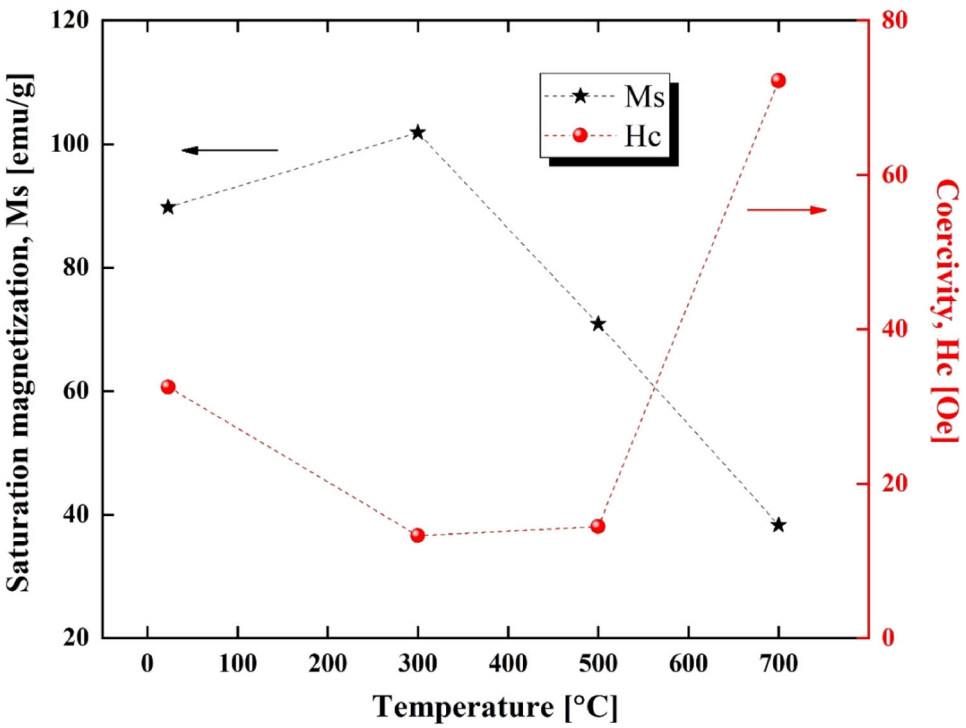

Fig. 11 Saturation magnetization and coercivity of the 50-h milled $Fe_{50}Ni_{10}Co_{10}Ti_{10}B_{20}$ HESM alloy powder at room temperature and heat treated at 300, 500, and 700 °C

solution of the elements without any contamination. The XRD analysis of 50-h milled $Fe_{50}Ni_{10}Co_{10}Ti_{10}B_{20}$ HESM alloy powder revealed the complete disappearance of the crystalline phases. The DTA curves showed the formation of crystallinity of the amorphous phase of the 50-h milled $Fe_{50}Ni_{10}Co_{10}Ti_{10}B_{20}$ HESM alloy powder. The increased Ms value (89.7 emu/g) in the 50-h milled $Fe_{50}Ni_{10}Co_{10}Ti_{10}B_{20}$ HESM alloy powder exhibits the amorphous phase. However, the decreased Hc value (32.5 Oe) indicates the soft magnetic character of the alloy. The heat treatment of the 50-h milled $Fe_{50}Ni_{10}Co_{10}Ti_{10}B_{20}$ HESM amorphous alloy powder at 300 °C increased the behavior of the saturation magnetization with high Ms value (101.9 emu/g) and reasonably less (38.3 emu/g) at 700 °C, which indicates full crystallization of the $Fe_{50}Ni_{10}Co_{10}Ti_{10}B_{20}$ HESM alloy. The Hc value was increased from 13.3 to 72.2 Oe while increasing the heat treatment temperature from 300 to 700 °C, with increase in the crystallite size. This displayed the prospective of the heat-treated amorphous $Fe_{50}Ni_{10}Co_{10}Ti_{10}B_{20}$ high entropy alloy as a functional soft magnetic material.

Acknowledgements

This work was supported by Scientific Research Projects Coordination Unit of Zonguldak Bülent Ecevit University, Project No. 2015-73338635-01.

References

1. N. Ma, S. Liu, W. Liu, L. Xie, D. Wei, L. Wang, L. Li, B. Zhao, Y. Wang, Research progress of titanium-based high entropy alloy: methods, properties, and applications. Front Bioeng Biotechnol **8**(1–18), 603522 (2020)
2. S. Gorsse, J.-P. Couzinié, D.B. Miracle, From high-entropy alloys to complex concentrated alloys. C. R. Physique **19**, 721–736 (2018)
3. B. Avar, T. Simsek, S. Ozcanc, A.K. Chattopadhyay, B. Kalkan, Structural stability of mechanically alloyed amorphous $(FeCoNi)_{70}Ti_{10}B_{20}$ under high-temperature and high-pressure. J. Alloys Compds. **860**(1–9), 158528 (2020)
4. N. Birbilis, S. Choudhary, J.R. Scully, M.L. Taheri, A perspective on corrosion of multi-principal element alloys. Npj Mater. Degrad. **5**(1–14), 14 (2021)
5. Y. Yin, J. Zhang, Q. Tan, W. Zhuang, N. Mo, M. Bermingham, M.-X. Zhang, Novel cost-effective Fe-based high entropy alloys with balanced strength and ductility. Mater. Des. **162**, 24–33 (2019)
6. L. Sang, Y. Xu, Amorphous behavior of $Zr_xFeNiSi_{0.4}B_{0.6}$ high entropy alloys synthesized by mechanical alloying. J. Non-Cryst. Solids **530**(1–7), 119854 (2020)
7. D.B. Miracle, O.N. Senkov, A critical review of high entropy alloys and related concepts. Acta Mater. **122**, 448–511 (2017)
8. M.-H. Tsai, J.-W. Yeh, High-entropy alloys: a critical review. Mater. Res. Lett. **2**(3), 107–123 (2014)
9. S.Y. Lee, S. Byeon, H.S. Kim, H. Jin, S. Lee, Deep learning-based phase prediction of high-entropy alloys: optimization, generation, and explanation. Mater. Des. **197**(1–16), 109260 (2021)
10. G.J. Naz, D. Dong, Y. Geng, Y. Wang, C. Dong, Composition formulas of Fe-based transition metals-metalloid bulk metallic glasses derived from dualcluster model of binary eutectic. Sci. Rep. **7**(1–11), 9150 (2017)
11. Z.-Q. Zhang, K.-K. Song, S. Guo, Q.-S. Xue, H. Xing, C.-D. Cao, F.-P. Dai, B. Völker, A. Hohenwarter, T. Maity, N. Chawake, J.-T. Kim, L. Wang, I. Kaban, J. Eckert, Optimizing mechanical properties of $Fe_{26.7}Co_{26.7}Ni_{26.7}Si_{8.9}B_{11}$ high entropy alloy by inducing hypoeutectic to quasi-duplex microstructural transition. Sci. Rep. **9**(1–14), 360 (2019)
12. Y. Zhang, M. Zhang, D. Li, T. Zuo, K. Zhou, M.C. Gao, B. Sun, T. Shen, Compositional design of soft magnetic high entropy alloys by minimizing magnetostriction coefficient in $(Fe_{0.3}Co_{0.5}Ni_{0.2})_{100-x}(Al_{1/3}Si_{2/3})x$ system. Metals **9**(1–12), 382 (2019)
13. M.E. McHenry, M.A. Willard, D.E. Laughlin, Amorphous and nanocrystalline materials for applications as soft magnets. Prog. Mater. Sci. **44**, 291–433 (1999)
14. A. Inoue, T. Zhang, H. Koshiba, A. Makino, New bulk amorphous Fe–(Co, Ni)–M–B (M=Zr, Hf, Nb, Ta, Mo, W) alloys with good soft magnetic properties. J. Appl. Phys. **83**, 6326–6328 (1998)
15. W. Li, P. Liu, P.K. Liaw, Microstructures and properties of high-entropy alloy films and coatings: a review. Mater. Res. Lett. **6**(4), 199–229 (2018)
16. H. Raanaei, V. Mohammad-Hosseini, Morphology and magnetic behavior of cobalt rich amorphous/nanocrystalline $(Co–Ni)_{70}Ti_{10}B_{20}$ alloyed powders. J. Magn. Magn. Mater. **414**, 90–96 (2016)
17. C. Suryanarayana, Mechanical alloying and milling. Prog. Mater Sci. **46**, 1–184 (2001)
18. T. Simsek, B. Avar, S. Ozcan, A.K. Chattopadhyay, B. Kalkan, Solid-state synthesis and characterization of the stable nanostructured $Ni_{21}Ti_2B_6$ phase. Phys. Status Solidi B **258**(5), 2000571 (2021)
19. C. Suryanarayana, E. Ivanov, in *Advances in Powder Metallurgy: Properties, Processing and Applications*, ed. by

I. Chang, Y. Zhao (Woodhead Publishing, Cambridge, 2013), p. 42
20. S. G. Sarwat, Contamination in wet-ball milling. Powder Metall. **60**(4), 267–272 (2017)
21. F.C. Li, T. Liu, J.Y. Zhang, S. Shuang, Q. Wang, A.D. Wang, J.G. Wang, Y. Yang, Amorphous–nanocrystalline alloys: fabrication, properties, and applications. Mater. Today Adv. **4**(1–20), 100027 (2019)
22. G. Herzer, Modern soft magnets: Amorphous and nanocrystalline materials. Acta Mater. **61**, 718–734 (2013)
23. K. Suzuki, G. Herzer, in *Advanced Magnetic Nanostructures*, ed. by D.J. Sellmyer, R. Skomski (Springer, Boston, 2006), p. 365
24. Y. Xu, Y. Sun, X. Dai, B. Liao, S. Zhou, D. Chen, Microstructure and magnetic properties of amorphous/nanocrystalline $Ti_{50}Fe_{50}$ alloys prepared by mechanical alloying. J. Mater. Res. Technol. **8**(3), 2486–2493 (2019)
25. R. Koohkan, S. Sharafi, H. Shokrollahi, K. Janghorban, Preparation of nanocrystalline Fe-Ni powders by mechanical alloying used in soft magnetic composites. J. Magn. Magn. Mater. **320**, 1089–1094 (2008)
26. G. Herzer, Grain size dependence of coercivity and permeability in nanocrystalline ferromagnets. IEEE Trans. Magn. **26**, 1397–1402 (1990)
27. H. Shokrollahi, The magnetic and structural properties of the most important alloys of iron produced by mechanical alloying. Mater. Des. **30**, 3374–3387 (2009)
28. A.H. Bahrami, H. Ghayour, S. Sharafi, Evolution of microstructural and magnetic properties of mechanically alloyed $Fe_{80-x}Ni_{20}Si_x$ nanostructured powders. Powder Technol. **249**, 7–14 (2013)
29. X. Wang, Q. Liu, Y. Huang, L. Xie, Q. Xu, T. Zhao, Effect of Ti content on the microstructure and corrosion resistance of $CoCrFeNiTi_x$ high entropy alloys prepared by laser cladding. Materials **13**(4–13), 2209 (2020)
30. S. Ma, J. Zhang, Wear resistant high boron cast alloy—a review. Rev. Adv. Mater. Sci. **44**, 54–62 (2016)
31. L. Zong, N. Guo, R. Li, H. Yu, Effect of B content on microstructure and wear resistance of Fe-3Ti-4C hardfacing alloys produced by plasma-transferred arc welding. Coatings **9**(2–11), 265 (2019)
32. C.P. Lee, Y.Y. Chen, C.Y. Hsu, J.W. Yeh, H.C. Shi, The effect of boron on the corrosion resistance of the high entropy alloys $Al_{0.5}CoCrCuFeNiB_x$. J. Electrochem. Soc. **154**(8), C424–C430 (2007)
33. A.N. Faruqui, P. Manikandan, T. Sato, Y. Mitsuno, K. Hokamoto, Mechanical milling and synthesis of Mg-SiC composites using underwater shock consolidation. Met. Mater. Int. **18**, 157–163 (2012)
34. Y.J. Liu, I.T.H. Chang, Effects of oxide phases on thermomagnetisation of mechanically alloyed amorphous Fe–(Co, Ni)–Zr–B powder. Mater. Sci. Eng. A **375–377**, 1092–1096 (2004)
35. N.D. Phu, D.T. Ngo, L.H. Hoang, N.H. Luong, N.H. Hai, Crystallization process and magnetic properties of amorphous iron oxide nanoparticles. J. Phys. D **44**(34), 345002 (2011)